JACS
JOURNAL OF THE AMERICAN CHEMICAL SOCIETY
Article
pubs.acs.org/JACS

Active Site Dependent Reaction Mechanism over Ru/CeO_2 Catalyst toward CO_2 Methanation

Fei Wang,[†] Shan He,[†] Hao Chen,[†] Bin Wang,[*,‡] Lirong Zheng,[§] Min Wei,[*,†] David G. Evans,[†] and Xue Duan[†]

[†]State Key Laboratory of Chemical Resource Engineering, Beijing University of Chemical Technology, Beijing 100029, P. R. China
[‡]Beijing Research Institute of Chemical Industry, Sinopec Group, Beijing 100013, P. R. China
[§]Institute of High Energy Physics, The Chinese Academy of Sciences, Beijing 100049, P. R. China

Supporting Information

ABSTRACT: Oxygen vacancy on the surface of metal oxides is one of the most important defects which acts as the reactive site in a variety of catalytic reactions. In this work, *operando* spectroscopy methodology was employed to study the CO_2 methanation reaction catalyzed by Ru/CeO_2 (with oxygen vacancy in CeO_2) and Ru/α-Al_2O_3 (without oxygen vacancy), respectively, so as to give a thorough understanding on active site dependent reaction mechanism. In Ru/CeO_2 catalyst, *operando* XANES, IR, and Raman were used to reveal the generation process of Ce^{3+}, surface hydroxyl, and oxygen vacancy as well as their structural evolvements under practical reaction conditions. The steady-state isotope transient kinetic analysis (SSITKA)-type *in situ* DRIFT infrared spectroscopy undoubtedly substantiates that CO_2 methanation undergoes formate route over Ru/CeO_2 catalyst, and the formate dissociation to methanol catalyzed by oxygen vacancy is the rate-determining step. In contrast, CO_2 methanation undergoes CO route over Ru surface in Ru/α-Al_2O_3 with the absence of oxygen vacancy, demonstrating active site dependent catalytic mechanism toward CO_2 methanation. In addition, the catalytic activity evaluation and the oscillating reaction over Ru/CeO_2 catalyst further prove that the oxygen vacancy catalyzes the rate-determining step with a much lower activation temperature compared with Ru surface in Ru/α-Al_2O_3 (125 vs 250 °C).

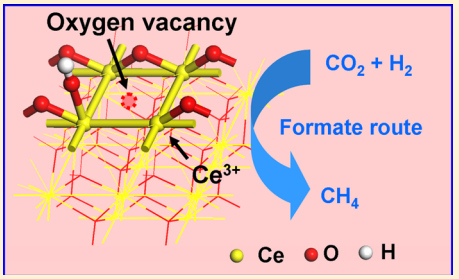

1. INTRODUCTION

The oxygen vacancy on the surface of CeO_2 is one of the most interesting catalytic structures in the field of heterogeneous catalysis.[1−4] In a variety of reactions (e.g., CO oxidation,[5,6] water gas shift reaction,[7,8] hydrogenation of CO/CO_2[9,10]), the oxygen vacancies participate in the catalytic process via two key routes: (1) storing and releasing oxygen,[11,12] and (2) promoting the dispersion degree and activity of supported noble-metal.[5,13] Great efforts have been made to develop novel catalysts with abundant oxygen vacancies in CeO_2 by various methods (e.g., crystal facets control[14−16] and doping[17−19]). However, detailed understanding on the critical role of oxygen vacancies in the reaction mechanism (e.g., reaction pathway and rate-determining step) is still deficient. The research in this area will shed light on the promotion effect of oxygen vacancies on catalytic reaction, which is beneficial to rational design and implementation for new types of heterogeneous catalysts.

The catalytic reactions which convert CO_2 to useful low-carbon fuels are very important elementary steps in C1 chemistry.[20,21] Especially, CO_2 methanation has become one research focus since it involves carbon recycle with fundamental research interest and potential environmental/commercial applications.[22,23] In the previous reports, CeO_2 supported Ru catalysts are recognized as promising catalysts in this reaction due to the abundant oxygen vacancies in CeO_2 which can greatly increase the reaction rate by adsorbing and activating the carbon−oxygen bond.[10,24,25] However, the knowledge of the intrinsic active site (e.g., Ru nanoparticles or CeO_2) and corresponding reaction mechanism (e.g., CO route or formate route) are still under controversy. Our previous work has shown that the surface oxygen vacancy rather than the metal in the Ru/CeO_2 catalytic system is the active site for CO_2 methanation.[10] However, this conclusion is based on the quantitative relation between the reaction rate and concentration of surface oxygen vacancies. The *operando* information on the active site dependent reaction mechanism is highly necessary to further push ahead the understanding of the decisive role of oxygen vacancies in this reaction.

The *operando* spectroscopy methodology for establishing the structure−activity/selectivity relationship has a significant impact on catalysis science in this decade, which inspires us to explore the detailed active site structure and reaction mechanism in CO_2 methanation.[26−28] Herein, we prepared Ru/CeO_2 catalyst (with oxygen vacancy) as the targeting sample and Ru/α-Al_2O_3 catalyst (without oxygen vacancy) as the control sample, so as to give a thorough understanding on active site dependent reaction mechanism. *Operando* XANES,

Received: March 15, 2016
Published: May 2, 2016

DOI: 10.1021/jacs.6b02762
J. Am. Chem. Soc. 2016, 138, 6298−6305

IR, and Raman were used to study the Ce^{3+}, surface hydroxyl, and oxygen vacancy in Ru/CeO_2 catalyst under the practical reaction conditions. The steady-state isotope transient kinetic analysis (SSITKA)-type *in situ* DRIFT infrared spectroscopy reveals that CO_2 methanation undergoes formate route on the surface of CeO_2 in which Ce^{3+}, surface hydroxyl, and oxygen vacancy jointly participate in this route. Especially, the formate dissociation catalyzed by oxygen vacancy is the rate-determining step. In contrast, CO_2 methanation undergoes CO route over $Ru/\alpha\text{-}Al_2O_3$ with the absence of oxygen vacancy. With the rapid advance of *operando* spectroscopy methodology, the identification of intrinsic active site and corresponding reaction mechanism will be an effective pathway for the design and preparation of high-performance heterogeneous catalysts.

2. EXPERIMENTAL SECTION

2.1. Materials. Chemical reagents including $Ce(NO_3)_3{\cdot}6H_2O$, $\alpha\text{-}Al_2O_3$, and $RuCl_3{\cdot}3H_2O$ were purchased from Sigma-Aldrich. Deionized water was used in all the experimental processes.

2.2. Preparation of CeO_2 Nanocubes. CeO_2 nanocubes were synthesized by a hydrothermal method similar to the previous report.[16] Typically, a NaOH solution (14 M, 30 mL) was added dropwise into a $Ce(NO_3)_3$ solution (0.113 M, 40 mL) with vigorous stirring at room temperature, followed by an additional stirring for 30 min with the formation of a milky slurry. The mixture was transferred into a 100 mL stainless-steel autoclave, tightly sealed, and hydrothermally treated at 180 °C for 24 h. The resulting precipitate was collected, washed thoroughly, and dried at 60 °C for 12 h, followed by a calcination process in muffle oven at 500 °C for 4 h to obtain the final CeO_2—NCs.

2.3. Preparation of Ru/CeO_2 and $Ru/\alpha\text{-}Al_2O_3$ Catalyst. The Ru/CeO_2 and $Ru/\alpha\text{-}Al_2O_3$ catalyst with Ru loading of 3 wt % were prepared by the precipitation deposition method. First, 3.0 g of support was suspended in 80 mL of water followed by adding 0.22 g of $RuCl_3{\cdot}3H_2O$. The suspension pH was adjusted to 8.0 with $NH_3{\cdot}H_2O$ aqueous solution (0.1 M) and the resulting suspension was aged at room temperature for 3 h with stirring. The precipitation obtained was separated by centrifugation, washed thoroughly, and dried at 60 °C for 12 h, followed by a calcination in air at 500 °C for 4 h. The obtained samples were denoted as RuO_2/CeO_2 and $RuO_2/\alpha\text{-}Al_2O_3$, respectively. Finally, the RuO_2/CeO_2 and $RuO_2/\alpha\text{-}Al_2O_3$ samples were reduced in a gaseous mixture of H_2 and N_2 (2:3, v/v) for 4 h at 400 °C with a heating rate of 5 °C min^{-1}, and the resulting catalysts were denoted as Ru/CeO_2 and $Ru/\alpha\text{-}Al_2O_3$, respectively.

2.4. Catalyst Characterization. The X-ray absorption near edge structure (XANES) spectroscopy was performed at the beamline 1W1B of the Beijing Synchrotron Radiation Facility (BSRF), Institute of High Energy Physics (IHEP), Chinese Academy of Sciences (CAS). The typical energy of the storage ring was 2.5 GeV with a maximum current of 250 mA. The Si (111) double crystal monochromator was used. The IFFEFIT 1.2.11 date analysis package (Athena, Artemis, Atoms, and FEFF6) was used for the date analysis and fitting. The infrared spectroscopy was recorded using a Vector22 (Bruker) spectrophotometer with 4 cm^{-1} of resolution. The Raman spectroscopy was recorded in a Jobin-Y'von LABRam HR800 microscope with a He—Ne green laser (532.14 nm). Elemental analysis of metal in samples was performed using a Shimadzu ICPS-7500 inductively coupled plasma emission spectrometer (ICP-AES). Transmission electron microscopy (TEM) observations were carried out on a JEOL JEM-2100 transmission electron microscope. Low-temperature N_2 adsorption—desorption isotherms of the samples were obtained on a Micromeritics ASAP 2020 sorptometer apparatus. All samples were outgassed prior to analysis at 200 °C for 12 h under 10^{-4} Pa vacuum. The total specific surface area was evaluated from the multipoint Brunauer—Emmett—Teller (BET) method. Temperature-programmed desorption (TPD) of the samples was performed by using a Micromeritics ChemiSorb 2720 with a thermal conductivity detector (TCD). Before measurement, the sample (100 mg) placed in a quartz U-tube reactor was degassed under flowing argon at 200 °C for 2 h. Then, the sample was reduced in the reactor in the gaseous mixture of H_2 and Ar (1:9, v/v) at 400 °C for 3 h. Subsequently, the reduced sample was purged in Ar at 500 °C for 30 min to remove excess hydrogen, then cooled down to 25 °C for readsorption of H_2; finally, a stream of argon (40 mL min^{-1}) was introduced to perform the TPD measurement with a temperature ramp of 10 °C min^{-1}. The dispersion of Ru was calculated based on the volume of chemisorbed H_2 using the following simplified equation:

$$D(\%) = \frac{2 \times V_{ad} \times M_{metal} \times SF}{m \times P \times V_m \times d_r} \times 100 \quad (1)$$

where m denotes the weight of sample (g); P is the weight fraction of Ru in the sample as determined by ICP; V_m is the molar volume of H_2 (22 414 mL mol^{-1}) at standard temperature and pressure (STP); d_r is the reduction degree of Ru; V_{ad} (mL) is the volume of chemisorbed H_2 at STP measured in the TPD procedure; M_{metal} is the molecular weight of Ru (101.07 g mol^{-1}); SF is the stoichiometric factor (Ru:H molar ratio in the chemisorption) which is taken as 1.

2.5. Evaluation of Catalytic Performance. The catalytic evaluation of the supported Ru catalysts for CO_2 methanation was carried out in a quartz tube reactor (8 mm in diameter) at atmospheric pressure. Brooks mass flow controllers were used to control the gas flow rate. To eliminate temperature and concentration gradient, 1.0 g of the catalyst was mixed with 1 mL of inert quartz sand (40—60 mesh; density: ~1.27g/mL) and then packed into the reactor. The reactor temperature was controlled by three thermocouples (located near the entrance, at the middle, and near the exit of the bed). After the catalyst pretreatment (see details in section 2.3), the reaction gas mixture consisting of CO_2 (15%, v/v), H_2 (60%, v/v), and Ar (25%, v/v) at 40 standard cubic centimeters per minute (sccm) total flow rate was introduced into the reactor, and the CO_2 conversion was measured in the temperature range 100—325 °C. The product gas stream was analyzed on line by gas chromatography (GC, Shimadzu, 2014C) equipped with a thermal conductivity detector (H_2, CO and CO_2) and a flame ionization detector (CH_4). The condensate was also analyzed by gas chromatography—mass spectrometry (GC—MS) off line.

3. RESULTS AND DISCUSSION

3.1. *Operando* Studies on the Detailed Structural Information on CeO_2 in Ru/CeO_2. In this work, three kinds of *operando* experimental approaches (XANES, IR, and Raman) were applied to give detailed structural information and corresponding structural changes during the catalytic reaction. XANES was used to obtain an insight into the Ce^{3+} structure. We measured the Ce L_3-edge XANES spectra of the catalyst during the reduction (Figure 1A) and reaction process (Figure 1B) within the temperature range from 25 to 400 °C at 10 °C/min; the reactor was maintained for 20 min at each specific selected temperature: 5 min for temperature stabilization, followed by 15 min for XANES analysis. For comparison, CeO_2 and CeF_3 are used as reference samples (Figure 1C). The Ce^{4+} compound (CeO_2) shows a double absorption line at the absorption edge (white line) at 5730 and 5737 eV, while the Ce^{3+} compound (CeF_3) displays a strong white line at 5726 eV.[29−31] A fit procedure with the reference samples (CeO_2 and CeF_3) was performed based on the spectra in Figure 1A,B. The spectrum was normalized using linear pre-edge and postedge, while the background was removed by spline fitting. Then, the Ce XANES (−20 to 60 E, eV) spectra were analyzed by linear combination fit (LCF) using the Athena software. For each spectrum, the combination of standards with the lowest residual parameter was chosen as the most likely set of components. The resulting Ce^{3+} percentage in CeO_2 as a function of temperature in the reduction and reaction process is given in

DOI: 10.1021/jacs.6b02762
J. Am. Chem. Soc. 2016, 138, 6298−6305

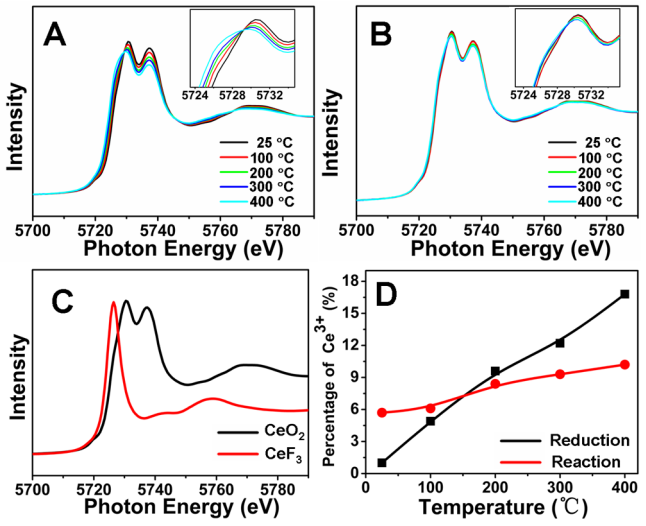

Figure 1. *Operando* XANES spectra of Ru/CeO_2 catalyst in (A) reduction process and (B) reaction process at different temperature. (C) XANES spectra of reference samples: CeO_2 and CeF_3. (D) Percentage of Ce^{3+} as a function of temperature in the reduction and reaction process, respectively.

Figure 1D. In the reduction process, the percentage of Ce^{3+} increases from 1.0% to 16.8% as the temperature rises from 25 to 400 °C, indicating the gradual transformation from Ce^{4+} to Ce^{3+}. Noticeably, in the reaction process, the percentage of Ce^{3+} declines significantly at 25 °C (from 16.8% to 5.7%), implying that a large portion of Ce^{3+} transforms to Ce^{4+} along with the introduction of CO_2. With the increase of reaction temperature, the percentage of Ce^{3+} remains at a much lower level compared with that in the reduction process. According to the previous report,[32] Ce^{3+} can act as Lewis base to adsorb CO_2, leading to the conversion from CO_2 to $CO_2^{\delta-}$ and the resulting Ce^{3+} to Ce^{4+}, which will be further discussed in the next section.

Operando FTIR transmission spectroscopy was used to characterize the surface hydroxyl on CeO_2 surface in the reduction process (Figure 2A) and reaction process (Figure 2B).[33] The measurement was conducted with the similar procedure in XANES. The peak intensity of the surface hydroxyl (3654 cm^{-1}) was measured as the quantitative index and was summarized in Figure 2C. In the reduction process, the peak intensity presents a volcanic rule which increases first from 25 to 250 °C and then decreases from 250 to 400 °C. This is probably due to the gradual generation process of surface hydroxyl and the thermal desorption effect at high temperature. In the reaction process, interestingly, the peak intensity of surface hydroxyl decreases sharply at 25 °C and maintains a much lower level from 50 to 400 °C. According to the previous report,[34] the surface hydroxyl is recognized as the structural basis involved in the hydrogen-spillover mechanism on the reducible supports.

The oxygen vacancies normally play an important role in the dissociation of oxygen-containing chemical bonds. Herein, we use *operando* Raman to monitor the concentration of oxygen vacancies in the reduction process (Figure 3A) and the subsequent reaction process (Figure 3B).[35] The relative peak intensity ratio between the defect-induced (D) mode peak (~570 cm^{-1}) and the first-order F_{2g} peak (~460 cm^{-1}) is related to the concentration of oxygen vacancy in CeO_2,[36,37] which is calculated and summarized in Figure 3C (I_D/I_{F2g}). In the reduction process, the I_D/I_{F2g} value increases from 0.02 to 0.52 as the temperature rises from 25 to 400 °C. This verifies the gradual generation of oxygen vacancies in the catalyst reduction process. However, when the reaction gas (CO_2 and H_2) is introduced into the reactor, this intensity ratio decreases sharply from 0.43 (at 25 °C) to 0.15 (at 100 °C), and keeps at a low level in temperature range 200−400 °C.

On the basis of the *operando* characterization methods above, the existence of Ce^{3+}, surface hydroxyl and oxygen vacancy is consolidated, and their structural evolvements under reaction conditions are revealed. In the reduction process, the gradual generation of these three structures and the reduction of Ru species are almost synchronous with the elevation of temperature (start at ~100 °C), whose structural evolvement mechanism is illustrated in Scheme 1. At first, the Ru species is reduced to metallic Ru, which provides the ability to dissociate H_2. Then, the dissociated hydrogen atom attacks Ce−O bond on CeO_2 surface, which generates the surface hydroxyl, Ce^{3+}, and oxygen vacancy. The hydrogen-spillover effect of metallic Ru would facilitate the attacking of hydrogen atom toward Ce−O bond on the substrate surface. In the reaction process, however, the concentrations of Ce^{3+} and surface hydroxyl decrease greatly at 25 °C, while the concentration of oxygen vacancy does not decrease until 100 °C. This phenomenon indicates that these three structures need different activation temperature and contribute in different elementary steps, which will be further discussed in the next section.

3.2. Active Site Dependent Reaction Mechanism in CO_2 Methanation. In the field of heterogeneous catalysis, especially for the multistep and structure-sensitive reaction systems, the reaction mechanism (e.g., the reaction intermediate and route) is highly correlated with the structure of the

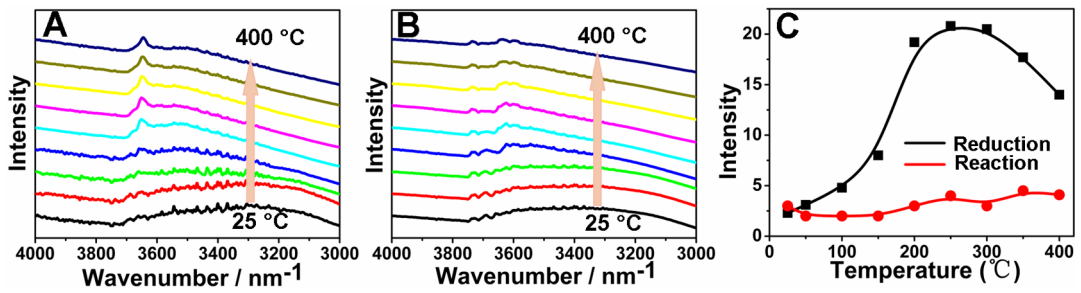

Figure 2. *Operando* FTIR transmission spectroscopy tested on Ru/CeO_2 in (A) the reduction process and (B) the reaction process. From bottom to top in each panel: 25, 50, 100, 150, 200, 250, 300, 350, and 400 °C. (C) The peak intensity of surface hydroxyl as a function of temperature in the reduction and reaction process.

DOI: 10.1021/jacs.6b02762
J. Am. Chem. Soc. 2016, 138, 6298−6305

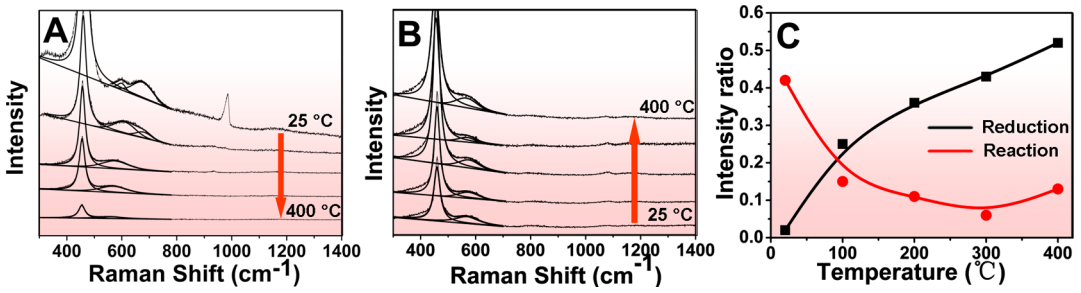

Figure 3. *Operando* visible Raman spectra of Ru/CeO_2 catalyst in (A) the reduction process and (B) the reaction process. The temperature points selected in each process: 25, 100, 200, 300, and 400 °C. (C) The corresponding I_D/I_{F2g} value as a function of temperature in the reduction and reaction process.

Scheme 1. Schematic Illustration of the Generation Process for Oxygen Vacancy, Ce^{3+}, and Surface Hydroxyl in Ru/CeO_2 Catalyst in the Reduction Process

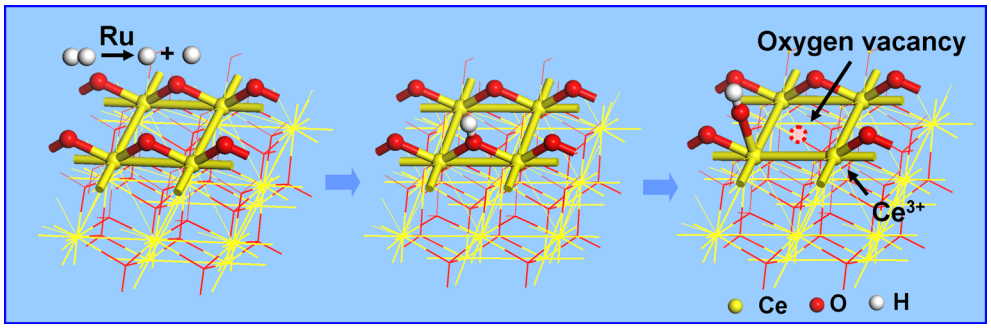

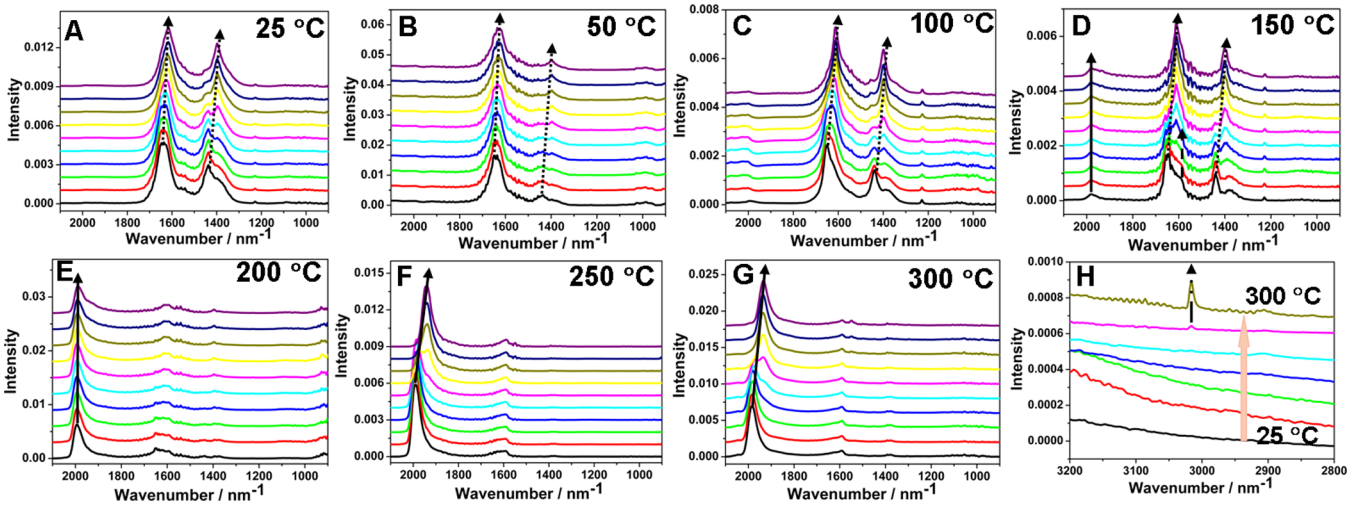

Figure 4. *Operando* DRIFT spectra recorded over $Ru/\alpha\text{-}Al_2O_3$ catalyst by introducing $^{13}CO_2$ and H_2 as reaction gas after 90 min of equilibrium reaction in $^{12}CO_2$ and H_2. From bottom to top in each panel: 0, 0.5, 1, 1.5, 2, 3, 5, 7, 10, and 15 min. From A to G: 25, 50, 100, 150, 200, 250, and 300 °C. (H) The DRIFT spectra of CH_4 recorded over $Ru/\alpha\text{-}Al_2O_3$ catalyst after 90 min of equilibrium reaction in $^{12}CO_2$ and H_2. From bottom to top: 25, 50, 100, 150, 200, 250, and 300 °C.

active sites.[38−40] To clarify the detailed catalytic roles of Ce^{3+}, surface hydroxyl, and oxygen vacancy for CO_2 methanation, we measured the steady-state isotope transient kinetic analysis (SSITKA) type *in situ* DRIFT infrared spectroscopy on Ru/CeO_2 catalyst (with these structures) as the targeting sample and $Ru/\alpha\text{-}Al_2O_3$ catalyst (without these structures) as the control sample. At one specific temperature, after 90 min of reaction process ($CO_2 + H_2$), CO_2 was replaced by the isotopic gas ($^{13}CO_2$) for 15 min for measurement. By correlating the buildup/decay of various surface species, we can obtain detailed information on the catalytic reaction mechanism. Figure 4 shows the SSITKA type *operando* DRIFT infrared spectra of $Ru/\alpha\text{-}Al_2O_3$ catalyst at seven specific temperatures from 25 to 300 °C (the TEM observation of $Ru/\alpha\text{-}Al_2O_3$ is shown in Figure S1). At 25 °C (Figure 4A), the characteristic signals of bicarbonate (1650 and 1439 cm^{-1}) are prominent when the catalytic system reaches the equilibrium state, showing that CO_2 converts to bicarbonate on $Ru/\alpha\text{-}Al_2O_3$ catalyst.[41] As $^{12}CO_2$ is replaced by $^{13}CO_2$, the characteristic bands of ^{12}C-bicarbonate diminish gradually, while new bands ascribed to ^{13}C-bicarbonate (1617 and 1399 cm^{-1}) are observed. However, no CH_4 or other species is found in the DRIFT infrared

DOI: 10.1021/jacs.6b02762
J. Am. Chem. Soc. 2016, 138, 6298−6305

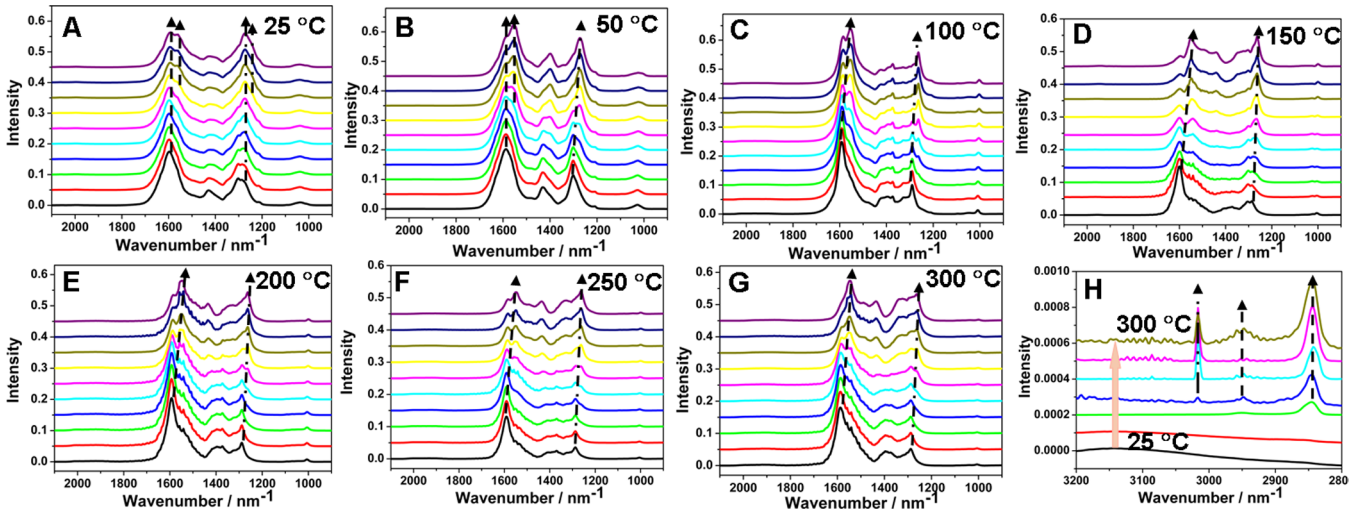

Figure 5. *Operando* DRIFT spectra recorded over Ru/CeO_2 catalyst by introducing $^{13}CO_2$ and H_2 as reaction gas after 90 min of equilibrium reaction in $^{12}CO_2$ and H_2. From bottom to top in each panel: 0, 0.5, 1, 1.5, 2, 3, 5, 7, 10, and 15 min. From A to G: 25, 50, 100, 150, 200, 250, and 300 °C. (H) The DRIFT spectra of CH_4 recorded over Ru/CeO_2 catalyst after 90 min of equilibrium reaction in $^{12}CO_2$ and H_2. From bottom to top: 25, 50, 100, 150, 200, 250, and 300 °C.

spectra, indicating that the peak shift of bicarbonate mainly results from thermal desorption rather than catalytic conversion. According to the previous reports,[42] the easy thermal desorption is due to the weak base property of α-Al_2O_3. For this reason, the peak intensities of bicarbonate become weaker and disappear finally at above 50 °C. From 150 to 300 °C, the characteristic signal of carbonyl (1990 cm^{-1}) is observed and enhances gradually. After the switching from $^{12}CO_2$ to $^{13}CO_2$, no obvious peak shift of carbonyl is found until the temperature rises to 250 °C. Interestingly, the characteristic signal of CH_4 (3017 cm^{-1}) also appears at the same temperature (Figure 4H), indicating that the activation temperature of carbonyl route for CO_2 methanation is 250 °C. Since the carbonyl is generally formed on metal surface, which is actually the chemisorbed CO, the Ru nanoparticles can be identified as the active site for CO route in this Ru/α-Al_2O_3 catalytic system.

In the case of Ru/CeO_2 catalyst, the SSITKA-type *operando* DRIFT infrared spectra show a more complicated reaction mechanism (Figure 5). On the one hand, carbonyl also appears at 150 °C and successfully converts to CH_4 at above 250 °C. This is attributed to the catalytic contribution of Ru nanoparticles (the same route as revealed in the Ru/α-Al_2O_3 system), which is not affected by the different metal dispersion and metal−support interaction in these two catalytic systems (Figure S2). On the other hand, more additional observations are obtained. When the catalytic system reaches the equilibrium state after 90 min of reaction, the characteristic signals of carboxylate ($CO_2^{\delta-}$, 1288 cm^{-1}) and formate (1593 cm^{-1}) are prominent at the whole temperature points. Different from the bicarbonate on Ru/α-Al_2O_3, first, CO_2 mainly converts to $CO_2^{\delta-}$ on Ru/CeO_2 catalyst which is more thermally stable (Scheme 2, Step 1).[32] This is likely due to the catalytic role of Ce^{3+} structure as Lewis base. The activation temperature for the conversion of Ce^{3+} to Ce^{4+} (25 °C, as shown by the *operando* XANES) exactly coincides with that for the conversion from CO_2 to $CO_2^{\delta-}$ (25 °C), which further verifies the catalytic role of Ce^{3+} in this elementary reaction. Subsequently, it is interesting that the activation temperature for the conversion of $CO_2^{\delta-}$ to formate (25 °C) agrees well with the starting temperature for the decrease of surface hydroxyl (25 °C, as

Scheme 2. Schematic Illustration of the Formate Route for CO_2 Methanation over the Ru/CeO_2 Catalyst[a]

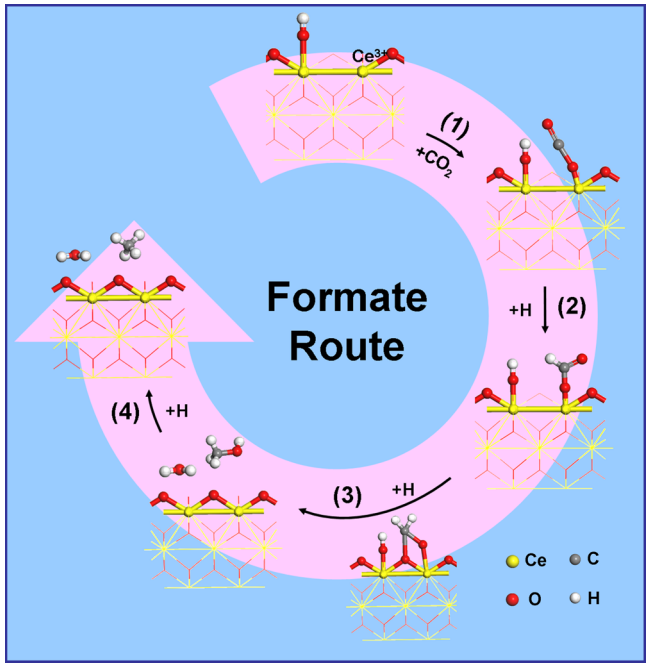

[a](1) Conversion of CO_2 to $CO_2^{\delta-}$, (2) hydrogenation of $CO_2^{\delta-}$ to formate, (3) dissociation of formate to methanol, (4) hydrogenation of methanol to CH_4.

shown by the *operando* IR). This proves that formate comes from the hydrogenation of $CO_2^{\delta-}$ assisted by the hydrogen in surface hydroxyl on CeO_2 surface (Scheme 2, Step 2).

As CO_2 is switched from $^{12}CO_2$ by $^{13}CO_2$, the characteristic bands of $^{12}C-CO_2^{\delta-}$ (1288 cm^{-1}) and ^{12}C-formate (1593 cm^{-1}) decrease gradually, while the corresponding new bands attributed to $^{13}C-CO_2^{\delta-}$ (1264 cm^{-1}) and ^{13}C-formate (1549 cm^{-1}) grow steadily. For $CO_2^{\delta-}$, a complete peak shift is achieved in 15 min at 50 °C. However, the peak shift of formate is not accomplished until 300 °C. At the same time, the characteristic bands of methanol (3659 and 1008 cm^{-1}, Figure

DOI: 10.1021/jacs.6b02762
J. Am. Chem. Soc. 2016, 138, 6298−6305

S3) were detected over Ru/CeO_2 catalyst in the reaction process, indicating that the dissociation of formate to methanol is the rate-determining step (Scheme 2, Step 3). Then, the hydrogenation of methanol to methane occurs easily in the final step (Scheme 2, Step 4).

The *operando* Raman spectra in the reaction process show that the concentration of oxygen vacancy remains at a high level at 25 °C and decreases sharply between 100 and 200 °C. This phenomenon indicates that oxygen vacancy is activated and participates in the CO_2 methanation reaction in this temperature range. SSITKA-type *in situ* DRIFT infrared spectroscopy reveals that both the transformation of formate and the successful production of CH_4 occur at the same temperature (150 °C, as shown in Figure 5, panels D and H, respectively). The results above confirm the critical role of oxygen vacancy in promoting the rate-determining step in the formate route. On the basis of the new observations, it is concluded that metal Ru serves as the active site for the CO route, while oxygen vacancy acts as the active site for the formate route (as shown in Scheme 2). This demonstrates an active site dependent reaction mechanism for CO_2 methanation. It should be noted that the activation temperature for formate route is much lower than that for the CO route (150 vs 250 °C), which shows the advantage of oxygen vacancy in promoting the rate-determining step. The catalytic role of oxygen vacancy in CO_2 methanation has also been reported previously.[24,43−45] Most of the studies focused on the relationship between the reaction activity and the oxygen vacancy structure; Leitenburg et al.[24] proposed that the oxygen vacancy plays an important role in the reduction of CO_2 to CO and/or surface carbonaceous species. However, the oxygen vacancy-dependent reaction mechanism is rarely discussed. Inspired by these reports, we carried out this *operando* spectroscopy investigation including XANES, IR, and Raman to quantitatively reveal the reaction mechanism of CO_2 methanation over oxygen vacancy.

To further establish the structure−property relationship, the catalytic activity of Ru/CeO_2 and $Ru/\alpha\text{-}Al_2O_3$ catalyst is evaluated in CO_2 methanation reaction. Figure 6A shows the

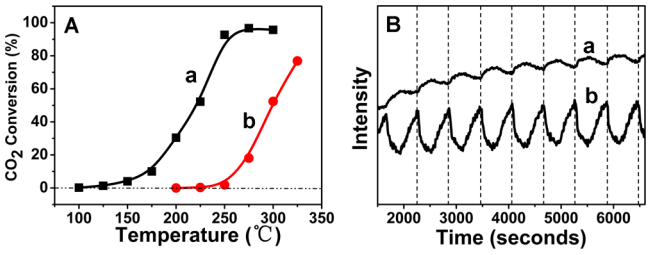

Figure 6. (A) The CO_2 conversion at steady state as a function of reaction temperature: (a) Ru/CeO_2, (b) $Ru/\alpha\text{-}Al_2O_3$. (B) Peak intensities of formate (1592 cm^{-1}, a) and methanol (3659 cm^{-1}, b) in CO_2 methanation over Ru/CeO_2 catalyst measured by *operando* DRIFT infrared spectroscopy every 10 s. The data of Ru/CeO_2 in panel A-a is cited from our previous work and reproduced with permission.[10] Copyright 2015, Elsevier.

CO_2 conversion vs reaction temperature over these two catalysts with CO_2 weight hourly space velocity (WHSV) of 360 mL g_{cat}^{-1} h^{-1}. For the sample of $Ru/\alpha\text{-}Al_2O_3$ (Figure 6A-b), the CO_2 conversion increases along with the enhancement of temperature and reaches 76.9% at 325 °C. In the case of Ru/CeO_2 catalyst (Figure 6A-a), however, the CO_2 conversion of 92.7% is obtained at 250 °C. The reaction rate over Ru/CeO_2 catalyst at 250 °C is 1.12×10^{-6} mol g_{cat}^{-1} s^{-1}, which is ~44 times higher than that over $Ru/\alpha\text{-}Al_2O_3$ catalyst at the same temperature (2.55×10^{-8} mol g_{cat}^{-1} s^{-1}, Table S1), demonstrating an excellent low-temperature-activity for the former catalyst. To further compare the real reaction activity in the presence of oxygen vacancy and Ru surface as the active site, we calculated the $TOF_{oxygen\ vacancy}$ at 175 °C for Ru/CeO_2 catalyst and TOF_{Ru} at 250 °C for $Ru/\alpha\text{-}Al_2O_3$ (Table S1). Despite the 75 °C lower reaction temperature, the TOF value on oxygen vacancy ($TOF_{oxygen\ vacancy}$: $(7.10 \pm 0.47) \times 10^{-4}$) is larger than that on Ru surface (TOF_{Ru}: $(6.93 \pm 0.51) \times 10^{-4}$), indicating that oxygen vacancy is a more desirable active site toward CO_2 methanation reaction. It should be noted that the activation temperature on Ru/CeO_2 and $Ru/\alpha\text{-}Al_2O_3$ catalyst is 125 and 250 °C, respectively, which approximately coincides with the activation temperature for formate route on Ru/CeO_2 (150 °C) and CO route on $Ru/\alpha\text{-}Al_2O_3$ (250 °C). The catalytic evaluation results agree with the active site-dependent reaction mechanism revealed by the *operando* spectroscopy method.

In addition, it is interesting that the peak intensities of formate (1592 cm^{-1}, a) and methanol (3659 cm^{-1}, b) in *operando* DRIFT infrared spectroscopy oscillate spontaneously at 150 °C under steady-state conditions with the introduction of a constant feed of the reaction gas (Figure 6B, reaction gas: CO_2 15%, H_2 60%, Ar 25%, v/v). The peak maximum of methanol is located at the antiphase in comparison with formate, confirming the production of methanol as a consequence of formate dissociation. It has been reported that for the oscillating chemical reaction, the reaction system should be far from the thermodynamic equilibrium.[46] This necessary condition is actually satisfied in this reaction system (CO_2 conversion below 4% at 150 °C). In a control experiment, when the reaction gas is replaced by a low concentration (CO_2 1%, H_2 4%, Ar 95%, v/v), the intensity oscillation disappears, indicating that the reaction system is close to thermodynamic equilibrium. More importantly, the oscillating chemical reaction often corresponds to a reversible structural change of the catalytic active site.[47] Taking into account the active site (oxygen vacancy) and rate-determining step (dissociation of formate to methanol) under this reaction condition (Ru/CeO_2 catalyst, 150 °C), it is proposed that the oscillatory chemical reaction is very likely related to the storing oxygen (Scheme 2, Step 3) and releasing oxygen (Scheme 1) process by oxygen vacancies.

In this work, the steady-state isotope transient kinetic analysis (SSITKA)-type *in situ* DRIFT infrared spectroscopy reveals that the "CO route" exists on both Ru/Al_2O_3 and Ru/CeO_2 catalyst, in which only Ru serves as the catalytic active site. Although the metal particle size and dispersion in these two systems are different, the "CO route" shows the similar reaction property (CO appears at 150 °C and converts to CH_4 at 250 °C). However, the "formate route" only occurs over the Ru/CeO_2 catalyst. The oxygen vacancy as active center catalyzes the rate-determining step at a much lower temperature compared with Ru in "CO route" (150 vs 250 °C). Moreover, due to the hydrogen-spillover undertaken by Ru nanoparticles, the active sites of "formate route" are located at the oxygen vacancies on the whole CeO_2 surface and do not limit to the metal−support interface. Therefore, the two reaction mechanisms of CO_2 methanation are dependent on different active sites (Ru surface or oxygen vacancy) toward rate-determining step.

DOI: 10.1021/jacs.6b02762
J. Am. Chem. Soc. 2016, 138, 6298−6305

4. CONCLUSIONS

In summary, we report an active site dependent catalytic mechanism toward CO_2 methanation by using Ru/CeO_2 and $Ru/\alpha\text{-}Al_2O_3$ catalyst. *Operando* XANES, IR, and Raman were employed to explore the generation process of Ce^{3+}, surface hydroxyl, and oxygen vacancy in Ru/CeO_2, and their structural evolvements under reaction conditions are clearly revealed. The steady-state isotope transient kinetic analysis (SSITKA)-type *in situ* DRIFT infrared spectroscopy verifies that all these three species participate in the catalytic process for the formate route in the presence of Ru/CeO_2, and oxygen vacancy catalyzes the formate dissociation to methanol, which is the rate-determining step. In contrast, metal Ru serves as the active site for the CO route in the $Ru/\alpha\text{-}Al_2O_3$ catalytic system. Moreover, the catalytic activity evaluation and the oscillating reaction on Ru/CeO_2 catalyst further prove that the oxygen vacancy catalyzes the rate-determining step with a much lower activation temperature compared with Ru surface in $Ru/\alpha\text{-}Al_2O_3$ system (125 vs 250 °C). This work provides a feasible strategy to uncover the intrinsic structure−activity correlation for the exploration of heterogeneous catalysts.

■ ASSOCIATED CONTENT

Supporting Information

The Supporting Information is available free of charge on the ACS Publications website at DOI: 10.1021/jacs.6b02762.

Additional experimental data (Figures S1−S3 and Table S1) (PDF)

■ AUTHOR INFORMATION

Corresponding Authors

*wangbin.bjhy@sinopec.com

*weimin@mail.buct.edu.cn

Notes

The authors declare no competing financial interest.

■ ACKNOWLEDGMENTS

This work was supported by the National Natural Science Foundation of China (NSFC) and the 973 Program (Grant No. 2014CB932104). M. Wei particularly appreciates the financial aid from the China National Funds for Distinguished Young Scientists of the NSFC.

■ REFERENCES

(1) Esch, F.; Fabris, S.; Zhou, L.; Montini, T.; Africh, C.; Fornasiero, P.; Comelli, G.; Rosei, R. *Science* **2005**, *309*, 752.

(2) Wang, Y.; Wang, F.; Song, Q.; Xin, Q.; Xu, S.; Xu, J. *J. Am. Chem. Soc.* **2013**, *135*, 1506.

(3) Vilé, G.; Bridier, B.; Wichert, J.; Pérez-Ramírez, J. *Angew. Chem., Int. Ed.* **2012**, *51*, 8620.

(4) Campbell, C. T.; Peden, C. H. F. *Science* **2005**, *309*, 713.

(5) Si, R.; Flytzani-Stephanopoulos, M. *Angew. Chem., Int. Ed.* **2008**, *47*, 2884.

(6) Kopelent, R.; Bokhoven, J. A.; Szlachetko, J.; Edebeli, J.; Paun, C.; Nachtegaal, M.; Safonova, O. V. *Angew. Chem., Int. Ed.* **2015**, *54*, 8728.

(7) Xu, W.; Si, R.; Senanayake, S. D.; Llorca, J.; Idriss, H.; Stacchiola, D.; Hanson, J. C.; Rodriguez, J. A. *J. Catal.* **2012**, *291*, 117.

(8) Karpenko, A.; Leppelt, R.; Plzak, V.; Behm, R. J. *J. Catal.* **2007**, *252*, 231.

(9) Spadaro, L.; Arena, F.; Granados, M. L.; Ojeda, M.; Fierro, J. L. G.; Frusteri, F. *J. Catal.* **2005**, *234*, 451.

(10) Wang, F.; Li, C.; Zhang, X.; Wei, M.; Evans, D. G.; Duan, X. *J. Catal.* **2015**, *329*, 177.

(11) Murugan, B.; Ramaswamy, A. V. *J. Am. Chem. Soc.* **2007**, *129*, 3062.

(12) Vivier, L.; Duprez, D. *ChemSusChem* **2010**, *3*, 654.

(13) Farmer, J. A.; Campbell, C. T. *Science* **2010**, *329*, 933.

(14) Liu, X.; Zhou, K.; Wang, L.; Wang, B.; Li, Y. *J. Am. Chem. Soc.* **2009**, *131*, 3140.

(15) Liu, L.; Yao, Z.; Deng, Y.; Gao, F.; Liu, B.; Dong, L. *ChemCatChem* **2011**, *3*, 978.

(16) Mai, H.; Sun, L.; Zhang, Y.; Si, R.; Wang, W.; Zhang, H.; Liu, H.; Yan, C. *J. Phys. Chem. B* **2005**, *109*, 24380.

(17) Montini, T.; Speghini, A.; Rogatis, L. D.; Lorenzut, B.; Bettinelli, M.; Graziani, M.; Fornasiero, P. *J. Am. Chem. Soc.* **2009**, *131*, 13155.

(18) Djinović, P.; Črnivec, I. G. O.; Erjavec, B.; Pintar, A. *Appl. Catal., B* **2012**, *125*, 259.

(19) Huang, Y.; Wang, A.; Li, L.; Wang, X.; Su, D.; Zhang, T. *J. Catal.* **2008**, *255*, 144.

(20) Wang, Z.; Xu, Z.; Peng, S.; Zhang, M.; Lu, G.; Chen, Q.; Chen, Y.; Guo, G. *ACS Catal.* **2015**, *5*, 4255.

(21) Liao, F.; Huang, Y.; Ge, J.; Zheng, W.; Tedsree, K.; Collier, P.; Hong, X.; Tsang, S. C. *Angew. Chem., Int. Ed.* **2011**, *50*, 2162.

(22) Wang, W.; Wang, S.; Ma, X.; Gong, J. *Chem. Soc. Rev.* **2011**, *40*, 3703.

(23) Aziz, M. A. A.; Jalil, A. A.; Triwahyono, S.; Ahmad, A. *Green Chem.* **2015**, *17*, 2647.

(24) Leitenburg, C.; Trovarelli, A.; Kašpar, J. *J. Catal.* **1997**, *166*, 98.

(25) Sharma, S.; Hu, Z.; Zhang, P.; McFarland, E. W.; Metiu, H. *J. Catal.* **2011**, *278*, 297.

(26) Bañares, M. A. *Catal. Today* **2005**, *100*, 71.

(27) Peterson, E. J.; DelaRiva, A. T.; Lin, S.; Johnson, R. S.; Guo, H.; Miller, J. T.; Kwak, J. H.; Peden, C. H. F.; Kiefer, B.; Allard, L. F.; Ribeiro, F. H.; Datye, A. K. *Nat. Commun.* **2014**, *5*, 4885.

(28) Wang, J.; Kispersky, V. F.; Delgass, W. N.; Ribeiro, F. H. *J. Catal.* **2012**, *289*, 171.

(29) Silversmit, G.; Poelman, H.; Balcaen, V.; Heynderickx, P. M.; Olea, M.; Nikitenko, S.; Bras, W.; Smet, P. F.; Poelman, D.; Gryse, R. D.; Reniers, M.; Marin, G. B. *J. Phys. Chem. Solids* **2009**, *70*, 1274.

(30) Sharma, A.; Varshney, M.; Shin, H.; Park, Y. J.; Kim, M.; Ha, T.; Chae, K. H.; Gautam, S. *Phys. Chem. Chem. Phys.* **2014**, *16*, 19909.

(31) Kumar, S.; Gautam, S.; Song, T. K.; Chae, K. H.; Jang, K. W.; Kim, S. S. *J. Alloys Compd.* **2014**, *611*, 329.

(32) Graciani, J.; Mudiyanselage, K.; Xu, F.; Baber, A. E.; Evans, J.; Senanayake, S. D.; Stacchiola, D. J.; Liu, P.; Hrbek, J.; Sanz, J. F.; Rodriguez, J. A. *Science* **2014**, *345*, 546.

(33) Xu, W.; Liu, Z.; Johnston-Peck, A. C.; Senanayake, S. D.; Zhou, G.; Stacchiola, D.; Stach, E. A.; Rodriguez, J. A. *ACS Catal.* **2013**, *3*, 975.

(34) Prins, R. *Chem. Rev.* **2012**, *112*, 2714.

(35) Lee, Y.; He, G.; Akey, A. J.; Si, R.; Flytzani-Stephanopoulos, M.; Herman, I. P. *J. Am. Chem. Soc.* **2011**, *133*, 12952.

(36) Trovarelli, A. *Catal. Rev.: Sci. Eng.* **1996**, *38*, 439.

(37) Martínez T, L. M.; Araque, M.; Centeno, M. A.; Roger, A. C. *Catal. Today* **2015**, *242*, 80.

(38) Crespo-Quesada, M.; Yarulin, A.; Jin, M.; Xia, Y.; Kiwi-Minsker, L. *J. Am. Chem. Soc.* **2011**, *133*, 12787.

(39) Hansen, T. W.; Wagner, J. B.; Hansen, P. L.; Dahl, S.; Topsøe, H.; Jacobsen, C. J. H. *Science* **2001**, *294*, 1508.

(40) Andersson, M. P.; Abild-Pedersen, F.; Remediakis, I. N.; Bligaard, T.; Jones, G.; Engbæk, J.; Lytken, O.; Horch, S.; Nielsen, J. H.; Sehested, J.; Rostrup-Nielsen, J. R.; Nørskov, J. K.; Chorkendorff, I. *J. Catal.* **2008**, *255*, 6.

(41) Wang, X.; Shi, H.; Kwak, J. H.; Szanyi, J. *ACS Catal.* **2015**, *5*, 6337.

(42) Cosimo, J. I. D.; Díez, V. K.; Xu, M.; Iglesia, E.; Apesteguía, C. R. *J. Catal.* **1998**, *178*, 499.

(43) Tada, S.; Shimizu, T.; Kameyama, H.; Haneda, T.; Kikuchi, R. *Int. J. Hydrogen Energy* **2012**, *37*, 5527.

(44) Tada, S.; Ochieng, O. J.; Kikuchi, R.; Haneda, T.; Kameyama, H. *Int. J. Hydrogen Energy* **2014**, *39*, 10090.

DOI: 10.1021/jacs.6b02762
J. Am. Chem. Soc. 2016, 138, 6298−6305

(45) Ussa-Aldana, P. A.; Ocampo, F.; Kobl, K.; Louis, B.; Thibault-Starzyk, F.; Daturi, M.; Bazin, P.; Thomas, S.; Roger, A. C. *Catal. Today* **2013**, *215*, 201.
(46) Imbihl, R.; Ertl, G. *Chem. Rev.* **1995**, *95*, 697.
(47) Hendriksen, B. L. M.; Ackermann, M. D.; Rijin, R.; Stoltz, D.; Popa, I.; Balmes, O.; Resta, A.; Wermeille, D.; Felici, R.; Ferrer, S.; Frenken, J. W. M. *Nat. Chem.* **2010**, *2*, 730.

DOI: 10.1021/jacs.6b02762
J. Am. Chem. Soc. 2016, 138, 6298−6305